

QRPA plus Phonon Coupling Model and the Photoabsorbtion Cross Section for $^{18,20,22}\text{O}$

G. Colò¹ and P.F. Bortignon

*Dipartimento di Fisica, Università degli Studi,
and INFN, Via Celoria 16, I-20133 Milano (Italy)*

ABSTRACT

We have calculated the electric dipole strength distributions in the unstable neutron rich oxygen isotopes $^{18,20,22}\text{O}$, in a model which include up to four quasi-particle-type configurations. The model is the extension, to include the effect of the pairing correlations, of a previous model very successful around closed shell nuclei, and it is based on the quasi-particle-phonon coupling. Low-lying dipole strength is found, which exhausts between 5 and 10% of the Thomas-Reiche-Kuhn (TRK) energy-weighted-sum-rule (EWSR) below 15 MeV excitation energy, in rather good agreement with recent experimental data. The role of the phonon coupling is shown to be crucial in order to obtain this result.

PACS numbers: 24.30.Cz, 21.60.Jz.

Keywords: low-lying dipole strength, giant resonances,
neutron-rich nuclei, quasi-particle RPA, phonon coupling.

¹ Tel.: + 39 - 02 - 58357261; fax: + 39 - 02 - 58357487; e-mail: colo@mi.infn.it

1 Introduction

The study of Giant Resonances (GR) in nuclei far from the stability line, such as halo and skin nuclei [1, 2], is still in its infancy. The observation of large E1 strength at low excitation energy, just above threshold in light drip-line nuclei, has produced strong excitement and large amount of activities, both experimental and theoretical. Electromagnetic dissociation measurements of this low-lying strength have been performed for the neutron halo nuclei ${}^6\text{He}$ [3], ${}^8\text{He}$ [4], ${}^{11}\text{Li}$ [5], ${}^{11}\text{Be}$ [6], ${}^{12}\text{Be}$ [7], ${}^{14}\text{Be}$ [8], ${}^{19}\text{C}$ [9], and for the proton halo nuclei ${}^8\text{B}$ [10] and ${}^{13}\text{O}$ [11]. From the theory side, a quantum-mechanical threshold effect was shown to enhance the transition strength from the loosely bound nucleons to the continuum [12, 13], essentially produced by the optimal matching of the wavelength of the scattering states with the large penetration length into the forbidden region of the weakly bound orbitals. In the case of two-nucleon halo nuclei, the enhancement due to the coherence in the transition amplitudes between the loosely bound nucleons, and also between these and the core, has been found important in recent shell-model calculations with the use of extended wave functions for the matrix elements of the dipole operator [14, 15] (see also [16]).

Moving to slightly heavier, eventually skin nuclei, the first attempt [17] of a systematic experimental study of GR has been recently performed at GSI, with the investigation of the dipole response of unstable neutron rich oxygen isotopes up to ${}^{22}\text{O}$ and to an excitation energy of 30 MeV. Use has been done of the electromagnetic excitation in heavy-ion collisions at around 600 MeV/u beam energy. Low-energy collective modes in ${}^{20}\text{O}$ were also measured recently for the first time by means of inelastic proton scattering [18].

Mean time, theoretical studies have been performed in the context of *mean-field* theories, like self-consistent Hartree-Fock and Random Phase Approximation (HF+RPA) calculations [19], eventually including exactly the crucial coupling to the continuum [20, 21], or HF-BCS plus quasi-particle RPA (QRPA) calculations [22] (which include the contribution of the pairing force), as well as relativistic RPA (RRPA) calculations [23], in order to investigate how the strength distributions of different multipole operators, in partic-

ular monopole, dipole and quadrupole, are evolving as one approaches the drip lines. The main features result to be: (a) the unusual concentration of multipole strength at the continuum threshold, already mentioned, when the threshold energy becomes of the order of one or few MeV, and (b) the strong interplay or mixing between the so-called isoscalar and isovector modes familiar from the response of stable nuclei.

Much less, and not at all systematically, has been done *beyond mean field*, that is, including the coupling of single-particle states to vibrational modes, in particular low-lying vibrations [24], as widely done in the case of stable nuclei in the last decades. Some pioneering works on the effects of this coupling on the single-particle self-energy and the GR strength function in neutron-rich nuclei are reported, e.g., in Refs. [25, 26, 27, 28, 29]. Of course, these correlations beyond mean field are also included, although somewhat hidden, in the shell-model calculations performed by several groups [30]. In particular, we mention the calculation of Ref. [31], where the dipole strength functions in the O isotopes were calculated, before the results of the GSI experiment quoted above were known.

Thus, it appears timely to extend in the present paper the microscopic model described in detail in Ref. [32] and aimed to a microscopic description of the excitation and decay of GR in stable nuclei, to the case of the neutron rich systems. This is done in the present work, where pairing correlations are included in the model in a simple way. The model is based on HF-RPA with Skyrme effective forces and includes on top escape and spreading effects in a consistent way. It was found to give accurate predictions, around closed shell nuclei, for the excitation energy and strength of GR as well as for widths and particle decay branching ratios [33].

The paper is organized as follows. In Section 2, the model and its extension are presented. The application to the calculation of the dipole strength functions in the O isotopes is described in Sect. 3, including also the comparison with the recent experimental data of Ref. [17] and with the shell-model results of Ref. [31]. Preliminary results were published in conference proceedings [34]. Summary and conclusions are drawn in Sect. 4.

2 Description of the model

In this section, we shortly present the extension of the model of Ref. [32], to include in a minimal way the effects of the pairing interaction. Indeed, we are interested to perform calculations along isotopes chains and the inclusion of pairing correlations is called for.

The starting input is an effective Hamiltonian H which includes a two-body interaction of the Skyrme type [35]. The self-consistent mean field is determined by solving the Hartree-Fock (HF) equations on a radial mesh, coupled with the standard BCS equations for the added pairing interaction (within the constant pairing gap approximation). This method is well known for spherical nuclei in the case of Skyrme interactions [35, 36]. The unoccupied states, at negative as well as positive energy, are determined by using a harmonic oscillator basis, so the continuum is discretized. This procedure defines a subspace labelled by Q_1 and including discrete two quasi-particle (2qp) configurations. The standard [37] QRPA equation in matrix form are solved on a basis of $J^\pi=1^-$ configurations belonging to Q_1 , to obtain collective (or non-collective) low-lying and GR modes (see also Ref. [22]). Special attention is paid to project out of the spectrum the spurious center-of-mass state, by renormalizing by a few percent the matrix elements of the residual interaction in such a way that the spurious state is pushed to zero energy.

To account for the spreading width Γ^\downarrow we build a second subspace Q_2 (the subspace P introduced in Ref. [32] to account for the escape width Γ^\uparrow is not included in the present model, see also next section). In Q_2 , there are the main configurations known [24] to play a major role in the damping process of GR: they are 2qp states coupled to a collective vibration calculated using the discrete QRPA in the Q_1 subspace as described above. We discuss in the next section what vibrations have been selected and included in Q_2 .

Using the projection operator formalism, it is easily found that the effects of coupling the subspace Q_2 to Q_1 are described by the following effective Hamiltonian \mathcal{H} acting in the Q_1 space

$$\begin{aligned} \mathcal{H}(E) &\equiv Q_1 H Q_1 + W^\downarrow(E) \\ &= Q_1 H Q_1 + Q_1 H Q_2 \frac{1}{E - Q_2 H Q_2 + i\epsilon} Q_2 H Q_1, \end{aligned} \tag{1}$$

where E is the excitation energy. For each value of E , the QRPA equations corresponding to this complex Hamiltonian $\mathcal{H}(E)$ are solved (this is done using the basis of the discrete QRPA states, eliminating those with negligible strength). The resulting sets of complex eigenstates $|\nu\rangle$ and eigenvalues $E_\nu - i\Gamma_\nu/2$, enable to calculate all relevant quantities, in particular the strength function $S(E)$ of the operator \hat{F} of interest:

$$S(E) = -\frac{1}{\pi} \text{Im} \sum_{\nu} \frac{\langle g.s. | \hat{F} | \nu \rangle^2}{E - E_\nu + i\Gamma_\nu/2}. \quad (2)$$

More in detail, each matrix element of $W^\downarrow(E)$ written in the basis of the discrete QRPA states is a linear combination of matrix elements $W_{\alpha\beta,\gamma\delta}^\downarrow(E)$ in the basis of the 2qp configurations $(\alpha\beta)$, $(\gamma\delta)$ etc. These latter matrix elements are sums of the eight terms depicted in Fig. 1. To evaluate these diagrams, we employ the following expression for the particle-vibration coupling Hamiltonian,

$$V = \sum_{\alpha\beta} \sum_{LnM} \langle \alpha | \varrho_n^{(L)}(r) v(r) Y_{LM}(\hat{r}) | \beta \rangle a_\alpha^\dagger a_\beta, \quad (3)$$

and we use the standard BCS expressions to relate the quasi-particle operators c_α^\dagger and c_α to the single-particle ones a_α^\dagger and a_α (see Eq. (12)). In Eq. (3) the vibration (phonon) $|n\rangle$ is characterized by its angular momentum L and its transition density $\varrho_n^{(L)}(r)$, while the form factor $v(r)$ is related to the particle-hole interaction V_{ph} derived from the Skyrme force as $V_{ph}(\vec{r}_1, \vec{r}_2) = v(r_1)\delta(\vec{r}_1, \vec{r}_2)$. The detailed expressions of the diagrams are given in the Appendix.

3 Application to the dipole response of $^{18-22}\text{O}$

We use the model discussed above to calculate the electric dipole strength distributions in the unstable neutron rich oxygen isotopes. As anticipated in the introduction, in a recent experiment [17] at GSI its knowledge has been extended to the isotopes heavier than ^{18}O , for which it was well known [38, 39], with systematic measurements from $A=17$ to $A=22$. Low-energy strength was detected, which exhausts up to 12% of the classical Thomas-Reiche-Kuhn (TRK) energy-weighted sum rule (EWSR) at excitation energies below 15 MeV (approximate threshold for the emission of the protons, which

are not detected in the experiment). The comparison with these data constitutes an adequate test for our model.

The calculations have been performed in the isotopes $^{18,20,22}\text{O}$, and using the effective force SIII [35]. This force, in the HF approximation, reproduces very well the binding energy of these nuclei (although it fails to fix the drip line for $Z=8$ at $A=24$). However, the corresponding self-consistent RPA description of the low-lying vibrations is rather poor in the comparison with the experimental data, and is improved by the inclusion of some pairing correlations [18, 22]. Therefore, we do include a pairing force with constant matrix elements of strength $G = 0.4$ MeV (about 30% of the standard value), and adopt the corresponding values of Δ_n for the neutrons in our constant gap calculation. These pairing gaps are smaller than 1 MeV (0.74, 0.79 and 0.21 MeV respectively in $^{18,20,22}\text{O}$), and the binding energies differ only by about 1% from the HF value. The $B(E2)$ values for the low-lying 2^+ states are somewhat improved compared to the RPA calculation (in the case of ^{20}O , the experimental value for the $B(E2)$ is 28 ± 2 e²fm⁴ [40], RPA gives only about 3 e²fm⁴ and our QRPA with the small gap gives 15.6 e²fm⁴).

The HF-BCS calculations are done in coordinate space, using a radial grid of 0.1 fm extending up to 15 fm. The use of a constant pairing gap Δ leads to unrealistic results unless a cutoff is introduced in the single-particle space, in such a way that states above this cutoff do not feel any pairing interaction: in our case, the cutoff is just above the $1d_{3/2}$ neutron state. In the QRPA calculations for the dipole and for the isoscalar modes to be included in the subspace Q_2 , the residual interaction between quasi-particles is derived from the Skyrme force without including the pairing contribution. The 2qp basis is chosen large enough so that the appropriate EWSR are satisfied. In the case of the dipole, we refer to the double commutator sum rule which is enhanced with respect to the classical TRK sum rule by a factor 1.33 in the case of the SIII interaction at hand.

In the QRPA calculation, the dipole strength below 15 MeV is found smaller than the experimental one (see Table 1). Then, the full coupling to the complex configurations of the Q_2 space is taken into account. The phonons included are those of multipolarity 1^- , 2^+ , 3^- and 4^+ which lie below 30 MeV and absorb more than 5% of the total strength. (In the case of ^{18}O , the 0^+ modes have been included but their effect is found to be

rather small). The final results for the integrated cross section up to 15 MeV is shown in Table 1 in comparison with the experimental data [17] and with the results of the shell-model calculation of [31]. The coupling with phonons increases the low-energy cross section, bringing it in rather good agreement with the data. Moreover, the drop of the cross section in ^{22}O is also reproduced. In the case of ^{18}O our results are also remarkably similar to the shell-model ones, suggesting that we are including the most important correlations.

The entire cross sections obtained with the full coupling for the three isotopes are displayed in Fig. 2. The progressive cumulation of cross section at lower energies with increasing A is evident, as well as the mild dependence on A of the main GDR peak and the appearance of more fragmented and peculiar structures at higher energies. In the case of ^{18}O , the peak energy at 24.2 MeV compares very well with the known experimental value [38], although the full experimental strength distribution looks wider (see Fig. 3(e) of [38]).

These features are not qualitatively very different in the calculations we performed with much larger pairing gap values, that is, the standard $12/\sqrt{A}$ MeV values. The results of these latter calculations are displayed in Fig. 3. In this case, compared to the calculation with the small gaps, the GDR main peak is more damped and the high energy structures more pronounced. The largest difference appears for the case of ^{22}O : moreover, in this nucleus the strength below 15 MeV is definitely larger than in the small gap case, at variance with $^{18,20}\text{O}$ where this strength is not very sensitive to the value of Δ_n we have employed (see Table 1). The fact that the GDR peak energy is not markedly affected by the size of the pairing gap in all cases can be understood since this is essentially ruled by mean field effects and at that level, the effect of pairing should not be important for states at energies much larger than $\approx 2\Delta$. Concerning the coupling with the phonons, for large values of the pairing gap, the low-energy surface vibrations become more collective but tend also to be pushed at higher energies (see also Fig. 1 of Ref. [22]) and these two facts have opposite consequences on the effectiveness of the phonon coupling. In the present case we understand from Fig. 3 that the first of these two effects (increased phonon collectivity) seems to be somewhat dominant.

We have not discussed so far the sensitivity of the results to the choice of the effective Skyrme force. An example can be seen in Fig. 4, where the full and dashed lines are two calculations for ^{18}O with the large gap, using respectively the forces SIII and SGII [41]. The difference between the two curves is essentially accounted for by a downward shift of about 2 MeV. This is mainly due to the different effective mass associated with the two interactions.

The most important outcome of our study is that the effect of the coupling with complex configurations including one phonon is very large and unavoidable if the comparison with experimental data is envisaged. The point is clearly emphasized in Fig. 5, for ^{18}O . The mean field (i.e., QRPA) result, with the simple smearing by means of 1 MeV width Lorentzian functions, are qualitatively altered when the coupling with phonons is included. This leads to a largely spread cross section, in much better agreement with the experiment. The effect is certainly larger than in stable, heavy nuclei, where most of our experience is. One main reason is the lack of the large cancellation [24] between the diagrams in the upper and lower two lines of Fig. 1. This is due to the very asymmetric phase-space available, in these light nuclei, for the hole-like and particle-like contributions to W^\downarrow and was already discussed in Ref. [42] for the shell-model calculation of the giant quadrupole resonance (GQR) in ^{16}O compared to ^{40}Ca . This asymmetry goes together, in hindering large cancellations, with the small number of components in the wave functions of the low-lying structures, as reported in Table 2 and in Table 3. Consequently, these structures should *not* be considered of collective nature.

Admittedly, this small number of components makes more critical than in the heavier nuclei the omission of the coupling to the continuum. The neutron separation energy in ^{22}O is still large, of the order of 7 MeV, but certainly the large role played in the wave functions by neutron quasi-particles like the $2p_{3/2}$ in the continuum poses some questions, worthwhile to be investigated. In any case, we show in Fig. 6 the results at the level of HF (that is, the unperturbed dipole strength function) obtained either taking properly the continuum into account or discretizing it. By choosing reasonable parameters to average the discrete results (see the caption to the figure) we reproduce very well the exact results, and this means that peak regions and corresponding intensities can be, in

this case, accounted for by the discrete calculation.

4 Conclusion

In the present work we have calculated the electric dipole strength distributions in the unstable neutron rich oxygen isotopes $^{18,20,22}\text{O}$. The model we used is the extension, to include the effect of the pairing correlations, of a previous model [32] which has been very successful around closed shell nuclei, and which is based on the quasi-particle-phonon coupling. Thus, the 2qp configurations of the standard QRPA approach, are coupled to 4qp-type configurations built with two uncorrelated quasi-particles plus a collective phonon (these are known to be particularly efficient in redistributing the GR strength).

Low-lying dipole strength is found, exhausting between 5 and 10% of the TRK sum rule below 15 MeV excitation energy, in rather good agreement with the recent experimental data of [17]. In order to obtain this result, and more generally to spread out the whole strength distribution including the main GDR peak, the role of the coupling with phonons appears to be crucial: therefore, the importance of particle-vibration coupling in neutron-rich nuclei is one of the most important outcomes of our paper. The comparison with the strength distributions obtained by means of large scale shell-model calculations [31] is satisfactory in terms of integrated quantities, especially in ^{18}O , although the detail of the distributions looks quite different.

Confident in our model, we are planning to apply it in the case of much heavier nuclei, relevant, e.g., for the study of the r-process and nucleosynthesis. In these nuclei, other types of microscopic calculations like the full shell-model may result prohibitive for computational reasons and, to describe the low-lying dipole strength, macroscopic models [43, 44] which may not contain all proper physical ingredients have been used so far [45].

Acknowledgments

We especially thank T. Aumann, H. Emling and A. Leistenschneider, for extensive communication and explanations about the detection of the low-lying dipole strength in the

oxygen isotopes. We also thank M. Thoenessen and Nguyen Van Giai for stimulating discussions. P.F.B. acknowledges RIKEN for financial support and nice hospitality during the period in which part of this work was performed, and the enlightening discussions about it with K. Ikeda.

Appendix

In this Appendix we provide the expressions of the eight diagrams contributing to the matrix element $W_{\alpha\beta,\gamma\delta}^\downarrow(E)$ mentioned in Sec. 2 and depicted in Fig. 1.

$$\begin{aligned}
W_I^\downarrow &= \delta(\alpha, \gamma)\delta(j_\beta, j_\delta)[1 + \delta(\alpha, \beta)]^{-1/2}[1 + \delta(\alpha, \delta)]^{-1/2}(2j_\beta + 1)^{-1} \sum_{\sigma, Ln} [1 + \delta(\alpha, \sigma)]^{-1/2} \\
&\quad (U_\beta U_\sigma + V_\beta V_\sigma)(U_\sigma U_\delta + V_\sigma V_\delta) \int dr u_\beta(r) u_\sigma(r) \varrho_n^{(L)}(r) v(r) \int dr u_\delta(r) u_\sigma(r) \varrho_n^{(L)}(r) v(r) \\
&\quad |\langle \beta || Y_L || \sigma \rangle|^2 \cdot [\omega - (E_\alpha + E_\sigma + \omega_n) + i\eta]^{-1}; \tag{4}
\end{aligned}$$

$$\begin{aligned}
W_{II}^\downarrow &= \delta(\alpha, \delta)\delta(j_\beta, j_\gamma)[1 + \delta(\alpha, \beta)]^{-1/2}[1 + \delta(\alpha, \gamma)]^{-1/2}(2j_\beta + 1)^{-1} \sum_{\sigma, Ln} [1 + \delta(\alpha, \sigma)]^{-1/2} \\
&\quad (U_\beta U_\sigma + V_\beta V_\sigma)(U_\sigma U_\gamma + V_\sigma V_\gamma) \int dr u_\beta(r) u_\sigma(r) \varrho_n^{(L)}(r) v(r) \int dr u_\gamma(r) u_\sigma(r) \varrho_n^{(L)}(r) v(r) \\
&\quad (-1)^{j_\alpha - j_\beta + J} |\langle \beta || Y_L || \sigma \rangle|^2 \cdot [\omega - (E_\alpha + E_\sigma + \omega_n) + i\eta]^{-1}; \tag{5}
\end{aligned}$$

$$\begin{aligned}
W_{III}^\downarrow &= \delta(\beta, \delta)\delta(j_\alpha, j_\gamma)[1 + \delta(\alpha, \beta)]^{-1/2}[1 + \delta(\beta, \gamma)]^{-1/2}(2j_\alpha + 1)^{-1} \sum_{\sigma, Ln} [1 + \delta(\beta, \sigma)]^{-1/2} \\
&\quad (U_\alpha U_\sigma + V_\alpha V_\sigma)(U_\sigma U_\gamma + V_\sigma V_\gamma) \int dr u_\alpha(r) u_\sigma(r) \varrho_n^{(L)}(r) v(r) \int dr u_\gamma(r) u_\sigma(r) \varrho_n^{(L)}(r) v(r) \\
&\quad |\langle \alpha || Y_L || \sigma \rangle|^2 \cdot [\omega - (E_\beta + E_\sigma + \omega_n) + i\eta]^{-1}; \tag{6}
\end{aligned}$$

$$\begin{aligned}
W_{IV}^\downarrow &= \delta(\beta, \gamma)\delta(j_\alpha, j_\delta)[1 + \delta(\alpha, \beta)]^{-1/2}[1 + \delta(\beta, \delta)]^{-1/2}(2j_\alpha + 1)^{-1} \sum_{\sigma, Ln} [1 + \delta(\beta, \sigma)]^{-1/2} \\
&\quad (U_\alpha U_\sigma + V_\alpha V_\sigma)(U_\sigma U_\delta + V_\sigma V_\delta) \int dr u_\alpha(r) u_\sigma(r) \varrho_n^{(L)}(r) v(r) \int dr u_\delta(r) u_\sigma(r) \varrho_n^{(L)}(r) v(r) \\
&\quad (-1)^{j_\alpha - j_\beta + J} |\langle \alpha || Y_L || \sigma \rangle|^2 \cdot [\omega - (E_\beta + E_\sigma + \omega_n) + i\eta]^{-1}; \tag{7}
\end{aligned}$$

$$\begin{aligned}
W_V^\dagger &= [1 + \delta(\alpha, \beta)]^{-1/2} [1 + \delta(\gamma, \delta)]^{-1/2} [1 + \delta(\alpha, \delta)]^{-1/2} (U_\alpha U_\gamma - V_\alpha V_\gamma) (U_\beta U_\delta - V_\beta V_\delta) \\
&\quad \sum_{Ln} \left\{ \begin{array}{ccc} j_\alpha & j_\beta & J \\ j_\delta & j_\gamma & L \end{array} \right\} \int dr u_\alpha(r) u_\gamma(r) \varrho_n^{(L)}(r) v(r) \int dr u_\beta(r) u_\delta(r) \varrho_n^{(L)}(r) v(r) \\
&\quad (-1)^{j_\beta + j_\gamma + J} \langle \alpha || Y_L || \gamma \rangle \cdot \langle \beta || Y_L || \delta \rangle \cdot [\omega - (E_\alpha + E_\delta + \omega_n) + i\eta]^{-1}; \tag{8}
\end{aligned}$$

$$\begin{aligned}
W_{VI}^\dagger &= [1 + \delta(\alpha, \beta)]^{-1} [1 + \delta(\gamma, \delta)]^{-1/2} (U_\beta U_\gamma - V_\beta V_\gamma) (U_\alpha U_\delta - V_\alpha V_\delta) \\
&\quad \sum_{Ln} \left\{ \begin{array}{ccc} j_\alpha & j_\beta & J \\ j_\gamma & j_\delta & L \end{array} \right\} \int dr u_\beta(r) u_\gamma(r) \varrho_n^{(L)}(r) v(r) \int dr u_\alpha(r) u_\delta(r) \varrho_n^{(L)}(r) v(r) \\
&\quad (-1)^{j_\beta + j_\gamma} \langle \alpha || Y_L || \delta \rangle \cdot \langle \beta || Y_L || \gamma \rangle \cdot [\omega - (E_\alpha + E_\beta + \omega_n) + i\eta]^{-1}; \tag{9}
\end{aligned}$$

$$\begin{aligned}
W_{VII}^\dagger &= [1 + \delta(\alpha, \beta)]^{-1/2} [1 + \delta(\gamma, \delta)]^{-1/2} [1 + \delta(\beta, \gamma)]^{-1/2} (U_\alpha U_\gamma - V_\alpha V_\gamma) (U_\beta U_\delta - V_\beta V_\delta) \\
&\quad \sum_{Ln} \left\{ \begin{array}{ccc} j_\alpha & j_\beta & J \\ j_\delta & j_\gamma & L \end{array} \right\} \int dr u_\alpha(r) u_\gamma(r) \varrho_n^{(L)}(r) v(r) \int dr u_\beta(r) u_\delta(r) \varrho_n^{(L)}(r) v(r) \\
&\quad (-1)^{j_\beta + j_\gamma + J} \langle \alpha || Y_L || \gamma \rangle \cdot \langle \beta || Y_L || \delta \rangle \cdot [\omega - (E_\beta + E_\gamma + \omega_n) + i\eta]^{-1}; \tag{10}
\end{aligned}$$

$$\begin{aligned}
W_{VIII}^\dagger &= [1 + \delta(\alpha, \beta)]^{-1/2} [1 + \delta(\gamma, \delta)]^{-1} (U_\beta U_\gamma - V_\beta V_\gamma) (U_\alpha U_\delta - V_\alpha V_\delta) \\
&\quad \sum_{Ln} \left\{ \begin{array}{ccc} j_\alpha & j_\beta & J \\ j_\gamma & j_\delta & L \end{array} \right\} \int dr u_\beta(r) u_\gamma(r) \varrho_n^{(L)}(r) v(r) \int dr u_\alpha(r) u_\delta(r) \varrho_n^{(L)}(r) v(r) \\
&\quad (-1)^{j_\beta + j_\gamma} \langle \alpha || Y_L || \delta \rangle \cdot \langle \beta || Y_L || \gamma \rangle \cdot [\omega - (E_\beta + E_\delta + \omega_n) + i\eta]^{-1}. \tag{11}
\end{aligned}$$

In the above expressions, σ labels an intermediate quasi-particle state, E and $u(r)$ indicate respectively the quasi-particle energy and the single particle radial wave function whereas U and V are the usual BCS coefficients which relate single particle and quasi-particle operators according to

$$c_\alpha^\dagger = U_\alpha a_\alpha^\dagger + V_\alpha a_{\bar{\alpha}}, \tag{12}$$

where $\bar{\alpha}$ is the time-reversed of α . Concerning the vibrational states (phonons), these are labelled by the multipolarity L and the index n : ω_n and $\delta \varrho_n^{(L)}(r)$ are the corresponding

energies and radial transition densities as already discussed in the text in Sec. 2 ($v(r)$ is also discussed there). The averaging parameter η is set at 0.5 MeV in the present calculation.

The above expressions are derived writing the single particle wave functions as $(u_{nl}(r)/r)i^l Y_{lm}(\hat{r})$ (phase convention II of Ref. [37]). In the limit of zero pairing gap, the expressions reported in Ref. [32] are recovered, where however, phase convention I of Ref. [37] without the factor i^l , was used.

References

- [1] I. Tanihata, J. Phys. G22 (1996) 157, and references therein.
- [2] P.G. Hansen, A.S. Jensen and B. Jonson, Ann. Rev. Nucl. Part. Sci. 45 (1995) 591.
- [3] T. Aumann *et al.*, Phys. Rev. C59 (1999) 1252.
- [4] Y. Iwata *et al.*, Phys. Rev. C62 (2000) 064311.
- [5] K. Ieki *et al.*, Phys. Rev. Lett. 70 (1993) 730; D. Sackett *et al.*, Phys. Rev. C48 (1993) 118; S. Shimoura *et al.*, Phys. Lett. B348 (1995) 29; M. Zinser *et al.*, Nucl. Phys. A619 (1997) 151.
- [6] T. Nakamura *et al.*, Phys. Lett. B331 (1994) 296
- [7] H. Iwasaki *et al.*, Phys. Lett. B491 (2000) 8.
- [8] M. Labiche *et al.*, Phys. Rev. Lett. 86 (2001) 600.
- [9] T. Nakamura *et al.*, Phys. Rev. Lett. 83 (1999) 1112.
- [10] T. Motobayashi *et al.*, Phys. Rev. Lett. 73 (1994) 2680; T. Kikuchi *et al.*, Eur. Phys. J. A3 (1998) 213; N. Iwasa *et al.*, Phys. Rev. Lett. 83 (1999) 2910.
- [11] T. Minemura *et al.*, Riken Accelerator Progress Report 33 (2000) 63.
- [12] P.G. Hansen and B. Jonson, Europhys. Lett. 4 (1987) 409.

- [13] F. Catara, C.H. Dasso and A. Vitturi, Nucl. Phys. A602 (1996) 181.
- [14] T. Suzuki, H. Sagawa and P.F. Bortignon, Nucl. Phys. A662 (2000) 282.
- [15] H. Sagawa, T. Suzuki, H. Iwasaki and M. Ishihara, Phys. Rev. C63 (2001) 034310.
- [16] H. Esbensen and G.F. Bertsch, Nucl. Phys. A542 (1992) 310.
- [17] T. Aumann *et al.*, Proc. of the Int. Conf. on Giant Resonances GR2000, Osaka, June 12-15, 2000, Nucl. Phys. A687 (2001) 103; A. Leistenschneider *et al.*, submitted.
- [18] E. Khan *et al.*, Phys. Lett. B490 (2000) 45.
- [19] F. Catara, E.G. Lanza, M.A. Nagarajan and A. Vitturi, Nucl. Phys. A614 (1997) 86; Nucl. Phys. A624 (1997) 449.
- [20] I. Hamamoto, H. Sagawa and X.Z. Zhang, Phys. Rev. C55 (1997) 2361; Phys. Rev. C56 (1997) 3121; Phys. Rev. C57 (1998) R1064.
- [21] H. Sagawa and H. Esbensen, Nucl. Phys. A (in press).
- [22] E. Khan and Nguyen Van Giai, Phys. Lett. B472 (2000) 253.
- [23] D. Vretenar, N. Paar, P. Ring and G.A. Lalazissis, Nucl. Phys. A (in press).
- [24] G.F. Bertsch, P.F. Bortignon and R.A. Broglia, Rev. Mod. Phys. 55 (1983) 287.
- [25] N. Vinh Mau, Nucl. Phys. A592 (1995) 33.
- [26] F. Ghielmetti, G. Colò, P.F. Bortignon and R.A. Broglia, Phys. Rev. C54 (1996) R2143.
- [27] G. Colò, P.F. Bortignon and R.A. Broglia, Nucl. Phys. A649 (1999) 335c.
- [28] G. Colò, T. Suzuki and H. Sagawa, submitted.
- [29] F. Barranco, R.A. Broglia, G. Colò and E. Vigezzi, nucl-th/0005073.

- [30] A. Poves and J. Retamosa, Phys. Lett. B184 (1987) 311; Nucl. Phys. A571 (1994) 221; E.K. Warburton, A. Becker and B.A. Brown, Phys. Rev. C41 (1990) 1147; S.E. Koonin, D.J. Dean and K. Langanke, Annu. Rev. Nucl. Part. Sci. 47 (1997) 463; Y. Utsuno, T. Otsuka, T. Mizusaki and M. Honma, Phys. Rev. C60 (1999) 054315.
- [31] H. Sagawa and T. Suzuki, Phys. Rev. C59 (1999) 3116.
- [32] G. Colò, Nguyen Van Giai, P.F. Bortignon and R.A. Broglia, Phys. Rev. C50 (1994) 1496.
- [33] G. Colò *et al.*, Phys. Lett. B276 (1992) 279; G. Colò and Nguyen Van Giai, Phys. Rev. C53 (1996) 2201; G. Colò *et al.*, Phys. Rev. C57 (1998) 3049.
- [34] G. Colò and P.F. Bortignon, Proc. of the Int. Conf. on Giant Resonances GR2000, Osaka, June 12-15, 2000, Nucl. Phys. A687 (2001) 282.
- [35] M. Beiner, H. Flocard, Nguyen Van Giai, Ph. Quentin, Nucl. Phys. A238 (1975) 29.
- [36] D. Vautherin, Phys. Rev. C7 (1973) 6.
- [37] D.J. Rowe, *Nuclear Collective Motion: Models and Theory*, Meuthen, London (1970).
- [38] J.G. Woodworth *et al.*, Phys. Rev. C19 (1979) 1667.
- [39] U. Kneissl *et al.*, Nucl. Phys. A272 (1976) 125.
- [40] S. Raman *et al.*, At. Data Nucl. Data Tables 36 (1987) 1.
- [41] N. Van Giai and H. Sagawa, Phys. Lett. B106 (1981) 379.
- [42] T. Hoshino and A. Arima, Phys. Rev. Lett. 37 (1976) 266.
- [43] Y. Suzuki, K. Ikeda and H. Sato, Prog. Theor. Phys. 83 (1990) 180.
- [44] P. Van Isacker, M.A. Nagarajan and D.D. Warner, Phys. Rev. C45 (1992) R13.
- [45] S. Goriely, Phys. Lett. B436 (1998) 10.

Fig. 1. Diagrams corresponding to the coupling of the 2qp configurations to the more complicated states including a phonon. See Sec. 2 for the discussion of this coupling, the detailed analytic expressions being given in the Appendix.

Fig. 2. Total photoabsorbtion cross section for the isotopic chain $^{18,20,22}\text{O}$ obtained within the full phonon coupling (using small pairing gaps as discussed in Sec. 3).

Fig. 3. Same as Fig. 2 in the case of large pairing gaps (i.e., $\Delta_n=12/\sqrt{A}$ MeV).

Fig. 4. Total photoabsorbtion cross section in the case of ^{18}O and of the large pairing gap, using two different effective forces namely SIII and SGII.

Fig. 5. Total photoabsorbtion cross section for ^{18}O . The large spreading induced by the coupling with the phonons included in the complete calculation (full line) contrasts with the sharp peaks of the QRPA result (dashed line). The integrals of the two curves over the entire range are respectively 303 and 320 MeV·mb.

Fig. 6. Unperturbed (i.e., Hartree-Fock) dipole strength obtained for ^{22}O either using the proper continuum (full line) or averaging (dashed line) the sharp peaks (bars) of the discretized continuum. For the averaging procedure, Lorentzian functions having width 2.2 MeV and 1.6 MeV have been employed, respectively for peaks below or above 12.5 MeV. Units are fm^2 for the bars and $\text{MeV}^{-1}\cdot\text{fm}^2$ for the lines.

Table 1: Total photoabsorbtion cross section integrated up to 15 MeV obtained in our QRPA (second row and third row) and QRPA plus phonon coupling (third and fourth row) calculations. The different choices for the pairing gap Δ_n (either small or large) are discussed extensively in the text. The results are compared with the photoneutron cross section measured at GSI (first row) and with the shell-model calculation of Ref. [31] (last row). All numbers are in MeV·mb.

	^{18}O	^{20}O	^{22}O
Experiment	22.14 ± 2.4	33.7 ± 3.5	23.22 ± 2.75
QRPA (small gap)	11.43	19.28	15.07
QRPA (large gap)	11.00	18.21	22.36
QRPA plus phonon coupling (small gap)	18.26	25.65	17.05
QRPA plus phonon coupling (large gap)	18.55	25.92	22.87
Shell model [31]	17.14	31.26	30.40

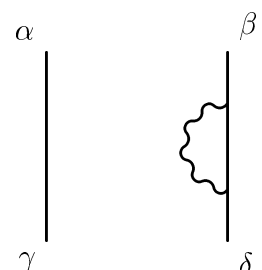
Table 2: Main components of the wave functions of the peaks around 12 MeV in $^{18,20}\text{O}$ (visible in Fig. 2). Only the real parts of the amplitudes which are larger in absolute value than 0.1, are reported. π and ν label the proton and neutron amplitudes, respectively.

	^{20}O	^{22}O
$\nu, 1p_{1/2} \ 2s_{1/2}$	0.82	0.83
$\nu, 1d_{5/2} \ 1f_{7/2}$	0.31	0.35
$\nu, 1d_{5/2} \ 2p_{3/2}$	-0.32	
$\pi, 1p_{1/2} \ 2s_{1/2}$	-0.18	
$\nu, 2s_{1/2} \ 2p_{3/2}$		0.30
$\nu, 2s_{1/2} \ 2p_{1/2}$		0.10

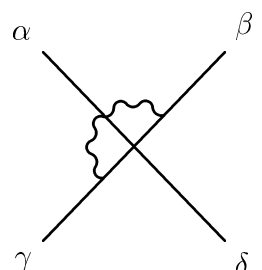
Table 3: Same as Table 1, in the case of the peak around 14.2 MeV in ^{20}O .

	^{20}O
$\nu, 1d_{5/2} \ 1f_{7/2}$	0.18
$\nu, 2s_{1/2} \ 2p_{3/2}$	-0.63
$\nu, 1p_{3/2} \ 1d_{5/2}$	-0.18

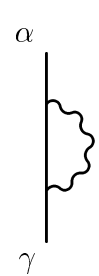
$$W_{\alpha\beta,\gamma\delta}^{\downarrow} =$$



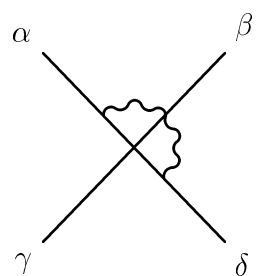
(I)



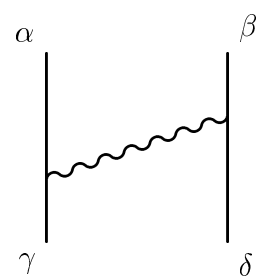
(II)



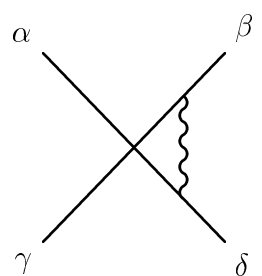
(III)



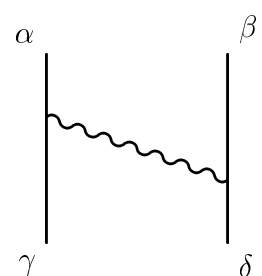
(IV)



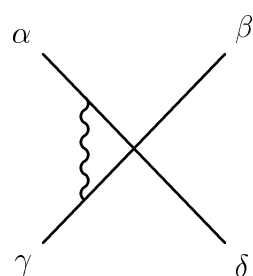
(V)



(VI)

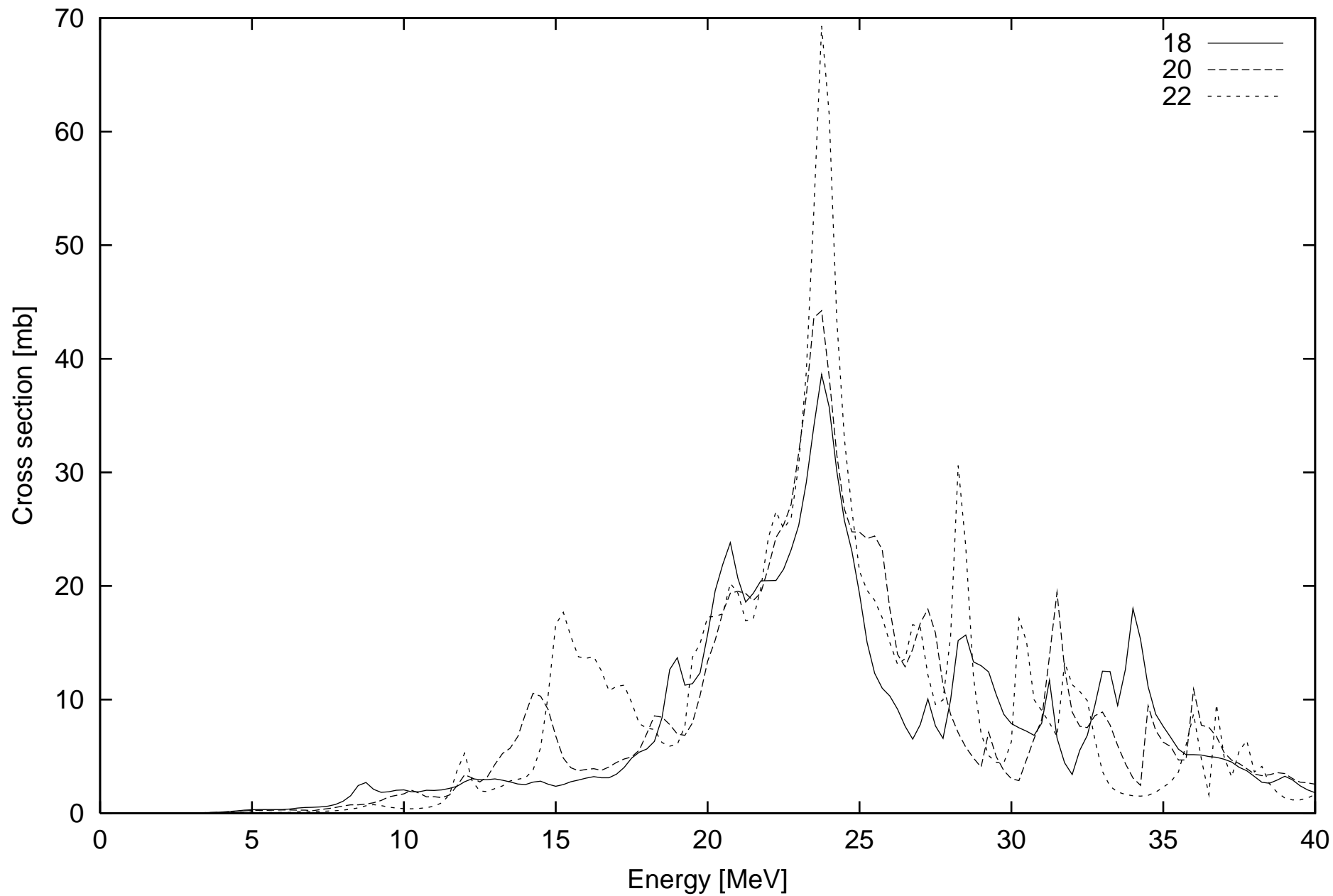


(VII)



(VIII)

Small gaps



Large gaps

